


Analogies between photochemical reactions and ground-state post-transition-state bifurcations shed light on dynamical origins of selectivity

Received: 3 April 2023

Accepted: 27 November 2023

Published online: 12 January 2024

 Check for updates

Zhitao Feng¹, Wentao Guo¹, Wang-Yeuk Kong¹, Dongjie Chen²,
Shunyang Wang¹ & Dean J. Tantillo¹✉

Revealing the origins of kinetic selectivity is one of the premier tasks of applied theoretical organic chemistry, and for many reactions, doing so involves comparing competing transition states. For some reactions, however, a single transition state leads directly to multiple products, in which case non-statistical dynamic effects influence selectivity control. The selectivity of photochemical reactions—where crossing between excited-state and ground-state surfaces occurs near ground-state transition structures that interconvert competing products—also should be controlled by the momentum of the reacting molecules as they return to the ground state in addition to the shape of the potential energy surfaces involved. Now, using machine-learning-assisted non-adiabatic molecular dynamics and multiconfiguration pair-density functional theory, these factors are examined for a classic photochemical reaction—the deazetization of 2,3-diazabicyclo[2.2.2]oct-2-ene—for which we demonstrate that momentum dominates the selectivity for hexadiene versus [2.2.2]bicyclohexane products.

How does one achieve kinetic selectivity? When tackling this problem, one is usually considering competing reactions with separate transition states (Fig. 1a) whose difference in free energy can be translated directly to an expected ratio of products; that is, one applies transition state theory¹. In some cases, however, transition state theory does not apply. For example, a large number of reactions have been found to proceed via ambimodal transition states, that is, transition states followed by steepest-descent pathways on potential energy surfaces (PESs) that bifurcate before reaching a secondary transition state that interconverts products (Fig. 1b)^{2–8}. In these reactions with post-transition-state bifurcations (PTSBs), a single transition state leads to competing products, so product ratios are controlled by non-statistical dynamic effects^{9–13}. Here we examine a third related scenario involving initial photoexcitation (Fig. 1c).

Photochemistry is often employed when a ground-state reaction faces an unsurmountable barrier (under a particular set of reaction conditions and/or in comparison to that for a competing undesired reaction)^{14–17}. Excitation of a reactant (described here as a single molecule, but really an ensemble) to a species with the same geometry as the ground-state species (that is, vertical or Franck–Condon excitation) generally lands one at a point that is not a minimum energy structure on the electronic excited-state surface. Consequently, the molecule in question will rapidly proceed downhill in energy, ultimately crossing back to the ground-state surface (perhaps crossing to one or more excited-state surfaces along the way). If the hop to the ground-state surface occurs near a ground-state transition state that interconverts the two competing products of interest (Fig. 1c)—not simply the reactant and one product, as is common—then selectivity is controlled

¹Department of Chemistry, University of California, Davis, Davis, CA, USA. ²Department of Electrical and Computer Engineering, University of California, Davis, Davis, CA, USA. ✉e-mail: djtantillo@ucdavis.edu

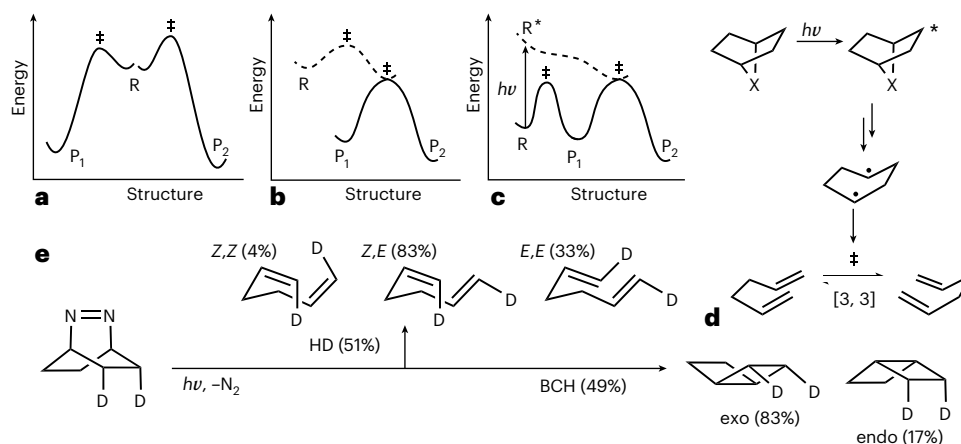


Fig. 1 | Analogies between ground-state and excited-state reactions.

a–c, Three routes to kinetic selectivity: transition state control (**a**), dynamic control via a PTSB (**b**) and dynamic control initiated by photochemical excitation (**c**). Note that the connection between the excited-state and ground-state surfaces is represented here as a point, but that is an oversimplification. R, reactant; P1, product 1; P2, product 2; R*, vertically excited reactant; ‡, transition structure; h , Planck's constant; ν , frequency. **d**, The initial design

plan involved photochemical removal of a group (X) to produce a diradical on an excited-state surface that resembles the transition structure for a [3, 3] sigmatropic shift. **e**, In this work, X=(N=N) was examined. Experimental results for this system^{40,41,44} are shown. On the arrows are shown the relative amounts of HD and BCH products. The relative amounts of different stereoisomers of each type of product (deduced from deuterium (D) labelling experiments) are shown on each structure.

by dynamic effects on the excited-state surface and the nature of surface hopping¹⁸.

This third scenario is similar to that of a reaction with a PTSB in that both scenarios involve approaching a transition state that interconverts competing products from 'above'. For a reaction with a PTSB, 'above' is from a higher energy transition state in the ground state. For the photo-promoted reaction just described, 'above' is from an excited state. In both cases, dynamic matching is at play^{13,19–22}; that is, the part of the energy released along the downhill pathway that is not lost to the solvent generates vibrationally excited 'hot' reactive species^{23–26}. The momentum associated with the process of falling downhill plays a role in determining the reaction outcome. Noting the analogy between reactions with PTSBs and photochemical reactions, we set out to design a reaction with energy surfaces akin to those in Fig. 1c. Our initial design plan involved reactions of the sort shown in Fig. 1d. Knowing that transition structures for Cope rearrangements can have significant diradical character^{27,28}, we examined a variety of systems that could produce cyclohexanediyls through loss of different X groups. Ultimately, we arrived at a classic system whose chemistry was in need of explanation: photochemical deazetization of 2,3-diazabicyclo[2.2.2]oct-2-ene (DBO; Fig. 1e). Modern modelling methods^{29–35}, coupled with our PTSB/non-statistical dynamic perspective, allowed us to answer some lingering questions for this archetypal system, providing a jumping off point for future design.

The photochemical reactivity of DBO has been studied under different reaction conditions (Fig. 1e). Grissom et al. investigated direct photolysis and reported a bicyclohexane (BCH; also called [2]-ladderane^{36–39}) to hexadiene (HD) ratio of 49:51 (refs. 39,40), which is consistent with results from other experiments^{41–43}. Edmunds and Samuel performed the photolysis of deuterium-labelled DBO⁴⁴, observing an excess (66%) of *exo*-BCH and determining the relative abundance of the HD isotopomers. Direct and sensitized DBO samples have also been shown to exhibit different reactivities, with more HD products observed and the *exo/endo* ratio being reduced to almost 1:1 for the latter⁴⁴.

Multiple attempts have been made to rationalize these product distributions. Chen and Li thoroughly investigated the first C–N bond dissociation process using high-precision multireference calculations that revealed a 12.2 kcal mol⁻¹ barrier for dissociation and a subsequent downhill process leading to a fourfold (S_0 – S_1 – T_1 – T_2 ; S, singlet; T, triplet)

crossing point⁴⁵. Their work successfully rationalized spectroscopic observations. Anderson and Grissom investigated the dependence of the product distribution on the solvent, temperature and magnetic field^{39,40}. They rationalized the product ratio based on the assumption of rapid intersystem crossing (ISC) and a statistical 25:75 distribution of singlet/triplet states. However, if ISC is rapid, we would expect a similar outcome for direct and sensitized reactions. Roberson and Simons explored this problem from the perspective of excess energy and conformations⁴⁶. They pointed out that the singlet–triplet gap becomes smaller along the reaction pathway, and singlet DBO behaves like triplet DBO at the singlet–triplet crossing point. However, they also noticed that unlike heavy-atom-containing solvents, magnetic field perturbation has no effect on the product ratio, leading them to question the effect of singlet–triplet interconversion^{39,40}. Heavy-atom tunnelling also has been found in chemical reactions involving diradical coupling and [3, 3] sigmatropic shifts, but that issue is not treated here^{47–50}.

Questions about DBO photochemistry still remain, however, that could be resolved with modern dynamics simulations. These types of simulations have only recently become feasible for tackling problems of the scope described here. In pioneering work, Martinez and coworkers used Born–Oppenheimer molecular dynamics (MD) simulations to investigate the photolysis of thioformaldehyde S-oxide sulfine, examining in detail how motion on the excited-state surface leads to ground-state products and pointing out that the complexity of photochemical reactions can arise from a single conical intersection⁵¹. Lopez and coworkers have used related methods to study a variety of photochemical organic reactions, including denitrogenation reactions of smaller frameworks²⁹.

However, conventional quantum-chemistry-based non-adiabatic MD (QC-NAMD) is very expensive and not practical for systems the size of DBO. Recently, Lopez and coworkers developed a machine-learning (ML)-based workflow for NAMD simulations (PyRAI²MD). This workflow aims to construct a ML potential through adaptive sampling and to conduct NAMD simulations. This approach has been used to study a variety of photochemical organic reactions and is able to reproduce key experimental data^{30,32–34}. For example, Li et al. have studied the formation of substituted cubanes via a photochemical [2 + 2] cycloaddition reaction, pointing out that dispersion interactions enhance the cycloaddition pathway³². These authors also studied the

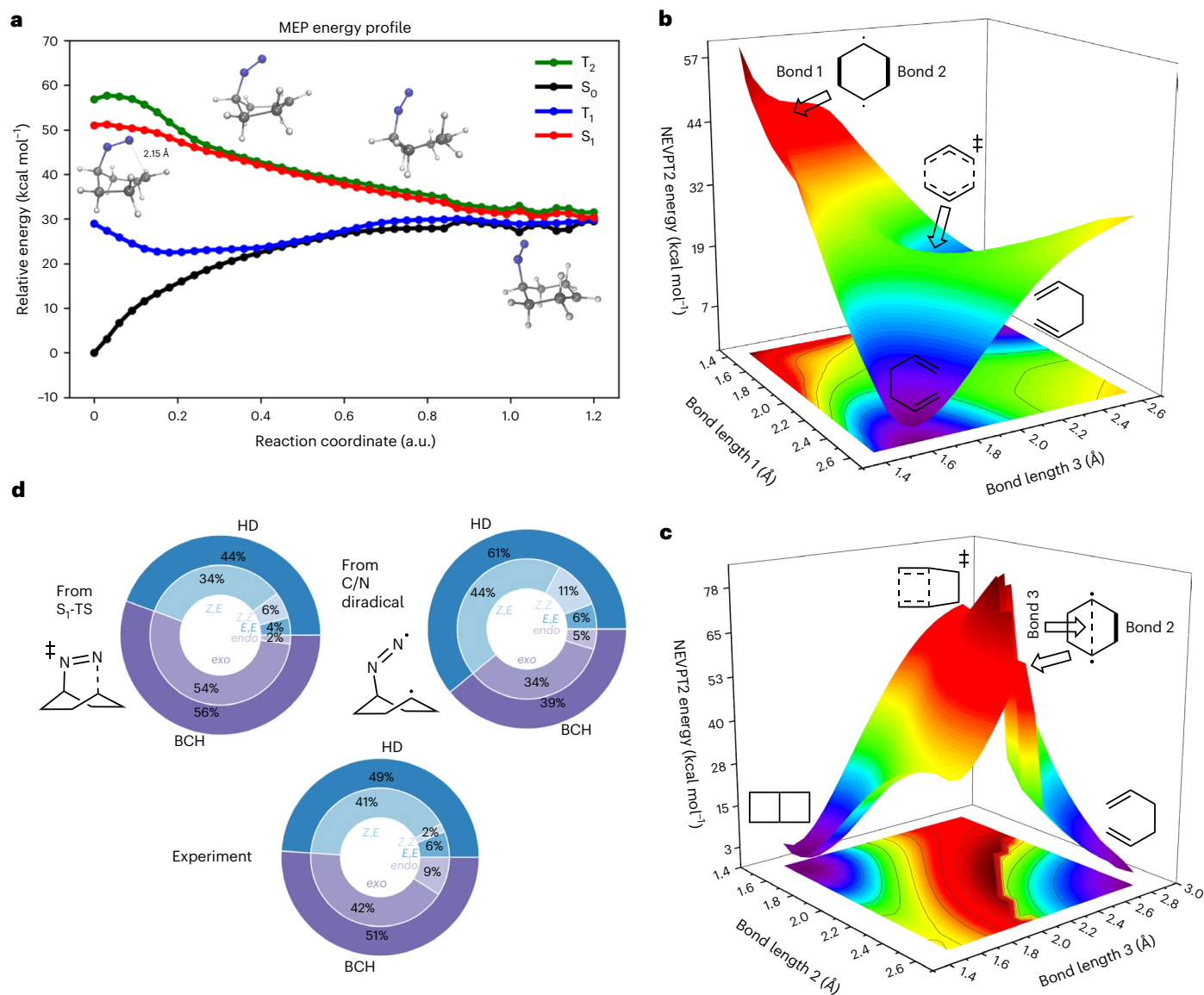


Fig. 2 | Photochemical reactivity of DBO. **a**, MEP starting from the transition structure for C–N bond dissociation on the S₁ surface computed at the CASPT2(8,8)/ANO-S-VDZP//revPBE(8,8)/ANO-S-VDZP level. The ‘0’ point of the MEP is defined as the S₀ energy of the corresponding transition structure. Relative energies are in kcal mol⁻¹. Insets show chemical structures. **b**, Portion of the S₀ PES adjacent to the 1,4-cyclohexanediyl showing the Cope rearrangement computed at the NEVPT2(6,6)/def2-TZVPP//SS-CASSCF(6,6)/def2-SVP level.

c, Portion of the S₀ PES adjacent to the 1,4-cyclohexanediyl showing the [2 + 2] cycloaddition computed at the NEVPT2(6,6)/def2-TZVPP//SS-CASSCF(6,6)/def2-SVP level. Insets in **b** and **c** show chemical structures at various parts of the surfaces. **d**, Comparison of ML-NAMD (top) and experimental (bottom) results. Note that initiating trajectories from the S₁-TS leads to a better match to the experimental HD/BCH ratio.

photochemical 4π-electrocyclization of different fluorobenzenes and showed that electrocyclization is promoted by momentum effects³³.

Here we use a combination of modern theoretical tools, that is, the ML-assisted NAMD (ML-NAMD) methods of Lopez et al.^{30,32–34} and the multiconfiguration pair-density functional theory (MC-PDFT)^{52–55} of Truhlar and Gagliardi, to interrogate DBO photochemistry at a new level of depth, allowing us to solve a long-standing reactivity/selectivity puzzle, thereby opening the door for forward design.

Results and discussion

Reaction pathway on the S₁ surface

Photoexcitation of DBO involves a typical n → π* transition. Calculations at the revPBE(8,8)/ANO-S-VDZP level reveal a vertical S₀–S₁ excitation energy of 87.2 kcal mol⁻¹ (3.78 eV), in reasonable agreement with experiment^{40,41} (76.4 kcal mol⁻¹ (3.31 eV); 80.5 kcal mol⁻¹ (3.49 eV) at

the CASPT2(8,8)/ANO-S-VDZP//revPBE(8,8)/ANO-S-VDZP level; refs. 56–60). Relaxation of DBO in the Franck–Condon region involves twisting the C–N=N–C bridge to form a minimum on the S₁ surface that is 3.6 kcal mol⁻¹ lower in energy⁴⁵ (CASPT2//MC-PDFT). Unlike many photochemical reactions, the photodissociation of DBO appears to involve a transition state for dissociation on the excited-state surface as a result of this facile relaxation process. The C–N-bond-breaking transition structure (S₁-TS) is associated with a barrier of 9.4 kcal mol⁻¹ (0.41 eV) on the S₁ surface, which is in reasonable agreement with the 8.6 kcal mol⁻¹ (0.37 eV) activation energy derived from kinetic experiments, as well as the low quantum yield and the observation of fluorescence⁴¹.

The minimum energy pathway (MEP) downhill from S₁-TS involves the elongation of one C–N bond. Proceeding through the geometries corresponding to the S₁ MEP, T₂ energies also decrease while S₀ and T₁

energies increase (Fig. 2a). Consequently, these four electronic states meet at the diazanyl diradical structure. Besides fast internal conversion, ISC also can, in principle, occur along this pathway^{61,62}. However, we have employed NAMD with MC-PDFT using the SHARC software (Supplementary Information for more details)^{63–66}, and although a small amount of ISC is observed, it is predicted to be inefficient and negligible. Given the massive additional computational resources required to accurately calculate spin–orbit coupling^{34,66}, here we focus on the direct photochemistry of DBO and the internal conversion between singlet states. As described later, we are able to rationalize the experimental outcome for direct photolysis by considering the fate of the S_1 state alone, suggesting that contributions from other states may be minor.

Although the diazanyl diradical is a minimum on the T_1 surface, we failed to locate a corresponding minimum on the S_1 or S_0 surface with MC-PDFT or complete active space second-order perturbation theory (CASPT2), likely, we suspect, a result of the flat PES region around the diazanyl diradical. A bond scan at the NEVPT2(6,6)/def2-TZVPP//SS-CASSCF(6,6)/def2-SVP level for S_0 shows that breaking of the second C–N bond, to form a 1,4-cyclohexanediyl, is nearly barrierless (Supplementary Fig. 7).

Justification for and implementation of ML-NAMD

As (a) hopping to the S_1 surface is expected to occur for the diazanyl diradical (that is, in the fourfold crossing region; Fig. 2a), (b) we find little to no barrier for loss of N_2 from the diazanyl diradical to form the 1,4-cyclohexanediyl, (c) our MEP calculation (Fig. 2a) indicates that the diradical forms via a very exothermic pathway and (d) we expect that intramolecular vibrational energy redistribution is likely slower than the subsequent reaction^{11,23–25}, dynamic matching can play a major role in determining product distributions^{1,13,19,20,23–25,67}. Consequently, we pursued fewest-switches surface hopping NAMD (FSSH-NAMD) simulations to determine the influence of non-statistical dynamic effects on the fate of the 1,4-cyclohexanediyl resulting from the paths leading to it^{30,34,68–71}.

Thus, our primary goal became identification of the reactivity of the 1,4-cyclohexanediyl. In previous studies, 1,4-cyclohexanediyls were proposed to be key intermediates along photochemical reaction pathways^{40,46}, and Stoltz and coworkers showed in a recent paper that a similar diradical resides on a flat energy surface with tiny barriers separating it from cycloaddition products⁷². We attempted to optimize the diradical at the CASPT2(4,4)/ANO-S-VDZP level of theory, but, to our surprise, the optimization converged to a transition structure for a [3, 3] sigmatropic shift (implying that such a diradical is not a minimum at this level). Calculations at the MC-PDFT level resulted in a similar conclusion. Broken-symmetry density functional theory (BS-DFT) and complete active space self-consistent field (CASSCF) optimizations, on the other hand, successfully located a 1,4-cyclohexanediyl intermediate in both chair and boat conformations. The sensitivity of the PES around the 1,4-cyclohexanediyl to the level of theory led us to examine the potential energy landscape of the diradical in more

detail. As shown in Fig. 2b,c, we performed two-dimensional scans of the forming/breaking bond lengths corresponding to the [3, 3] sigmatropic shift and a [2 + 2] cycloaddition connected to the BCH product. While CASSCF revealed a shallow minimum for the diradical (Supplementary Fig. 8), NEVPT2//CASSCF single-point energies led to the minimum region vanishing for both PESs. In both cases, the diradical resides on a flat region of the PES that connects to the [3, 3] sigmatropic shift transition structure and [2 + 2]-cycloaddition transition structure.

Given the various products formed upon DBO photoexcitation, it seems likely that multiple reaction events occur after the first C–N-bond-breaking transition state and subsequent flat region of the PES. As competing transition structures leading to different products do not appear to exist, rationalization of the product distribution is, of course, difficult. Dealing with this scenario is difficult for ground-state surfaces^{1,2,6}, but is even more difficult here when species must cross between excited-state and ground-state surfaces. And, to make matters worse, according to our CASPT2//MC-PDFT computations and previous literature, the S_0 – S_1 energy gap around the diazanyl diradical is small, indicating the feasibility of internal conversion at this critical structure. Taken together, these factors strongly suggest that NAMD simulations are necessary for the rationalization of product distributions in such a case.

Here we employed the ML-NAMD approach of Lopez et al. (Methods and Supplementary Information for details)^{30,32–34}, initiated from different points along our computed MEP. Some 3,600 trajectories were obtained for each NAMD task. The ML-NAMD results are summarized in Fig. 2d. For the ensemble of trajectories initiated from the C–N-dissociation transition structure (S_1 state at 300 K; Fig. 2d, left), 45% of the reactive trajectories form the HD product, while 56% form the BCH product, which is consistent with the product distribution observed in the experiment by Grissom et al. (Fig. 2d, bottom)^{39,40}. Among all the HD-forming trajectories, the Z,E isomer is predicted to dominate (76%), again consistent with experiment (83% based on isotopic labelling)⁴⁴. In addition, a significant excess of *exo* product (96%) is observed, again consistent with experiment (83%)^{39,40}.

To investigate how initial momentum and geometry affects the reaction outcome, we also ran trajectories at different temperatures and with different initial geometries. The product distribution was found to be almost independent of the temperature and initial geometry on the MEP, except for trajectories initiated from the diazanyl diradical, which lead to 17% more HD product (Fig. 2d, right). Note that the excess of HD product is not consistent with experiment, implying that a non-statistical dynamic effect associated with approaching the diazanyl diradical specifically from the C–N-dissociation transition structure may play an important role.

As expected, we observe that most of the ML-NAMD trajectories hop back to S_0 in the region of the diazanyl diradical, that is, at the fourfold crossing region where the S_0 , S_1 , T_1 and T_2 states are almost degenerate (Fig. 2a and Supplementary Fig. 5). Due to the efficient

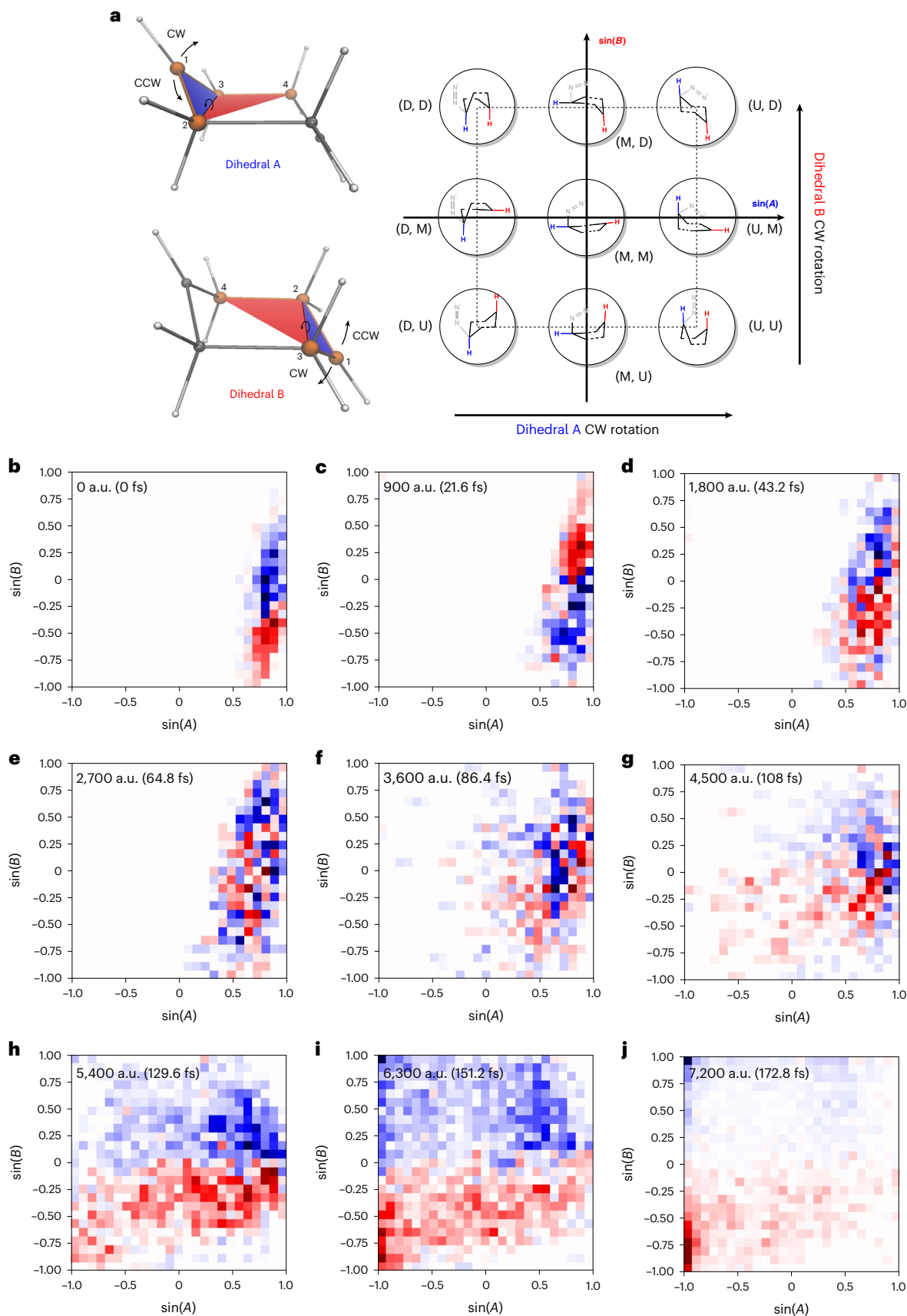
Fig. 3 | Momentum effects. **a**, A graphical depiction of the dihedral angle space of the 1,4-cyclohexanediyl, with chemical structures at the left. For a better demonstration of how the second C–N bond dissociation affects dihedral angle A , the position of the diazo group from the previous step is shown. **b–j**, The population difference of the dihedral angle for 2,072 ML-NAMD trajectories forming *exo*-BCH and *Z,E*-HD. We define the population density ρ as the number of trajectories passing through the dihedral angle grid at one certain time step. The population density difference is the subtraction of the BCH-forming density from the HD-forming density ($\Delta\rho = \rho_{\text{BCH}} - \rho_{\text{HD}}$). Red colour indicates that the number of HD-forming trajectories exceeds that of BCH-forming trajectories, and vice versa for blue. The population difference is scaled to $[-1, 1]$ and a two-slope normalization is employed. White colour indicates that either the number of BCH-forming and the number of HD-forming trajectories are equal, or

no trajectories populate this grid. Due to the facts that the minimum and maximum of the population difference are not symmetrically distributed on both sides of zero, and that the minimum and maximum values are not the same in each picture, we need to scale the plots with different parameters to make sure that white colour always indicates an equal amount of BCH and HD trajectories ($\Delta\rho = \rho_{\text{BCH}} - \rho_{\text{HD}} = 0$). To do so, we map the population density difference of grid a ($\Delta\rho_a$) to $2 \frac{\Delta\rho_a - \Delta\rho_{\text{min}}}{\Delta\rho_{\text{max}} - \Delta\rho_{\text{min}}} - 1$. By doing so, all mapped data fall into the range of $[-1, 1]$. The equivalent point (Eq, equal BCH and HD density) is mapped to $\text{Eq} = \frac{-2\Delta\rho_{\text{min}}}{\Delta\rho_{\text{max}} - \Delta\rho_{\text{min}}} - 1$. However, Eq is still not the middle point, because generally $|\Delta\rho_{\text{max}}| \neq |\Delta\rho_{\text{min}}|$. Thus, we employed a two-slope normalization of the data. The conceptual centre, Eq, is placed at the centre of the colour bar, and the two sides are normalized differently. $\sin(A)$ and $\sin(B)$ are the sin of angle A or B .

internal conversion rate, subsequent reaction events occur on the ground-state S_0 surface. Thus, we now turn our attention to the issue of momentum effects on the 1,4-cyclohexanediyl formed after surface hopping.

Dynamic properties of the 1,4-cyclohexanediyl

Detailed analysis of the trajectories, which lead to an outcome consistent with the known experimental results, allows us to evaluate the means by which momentum influences the conformational dynamics



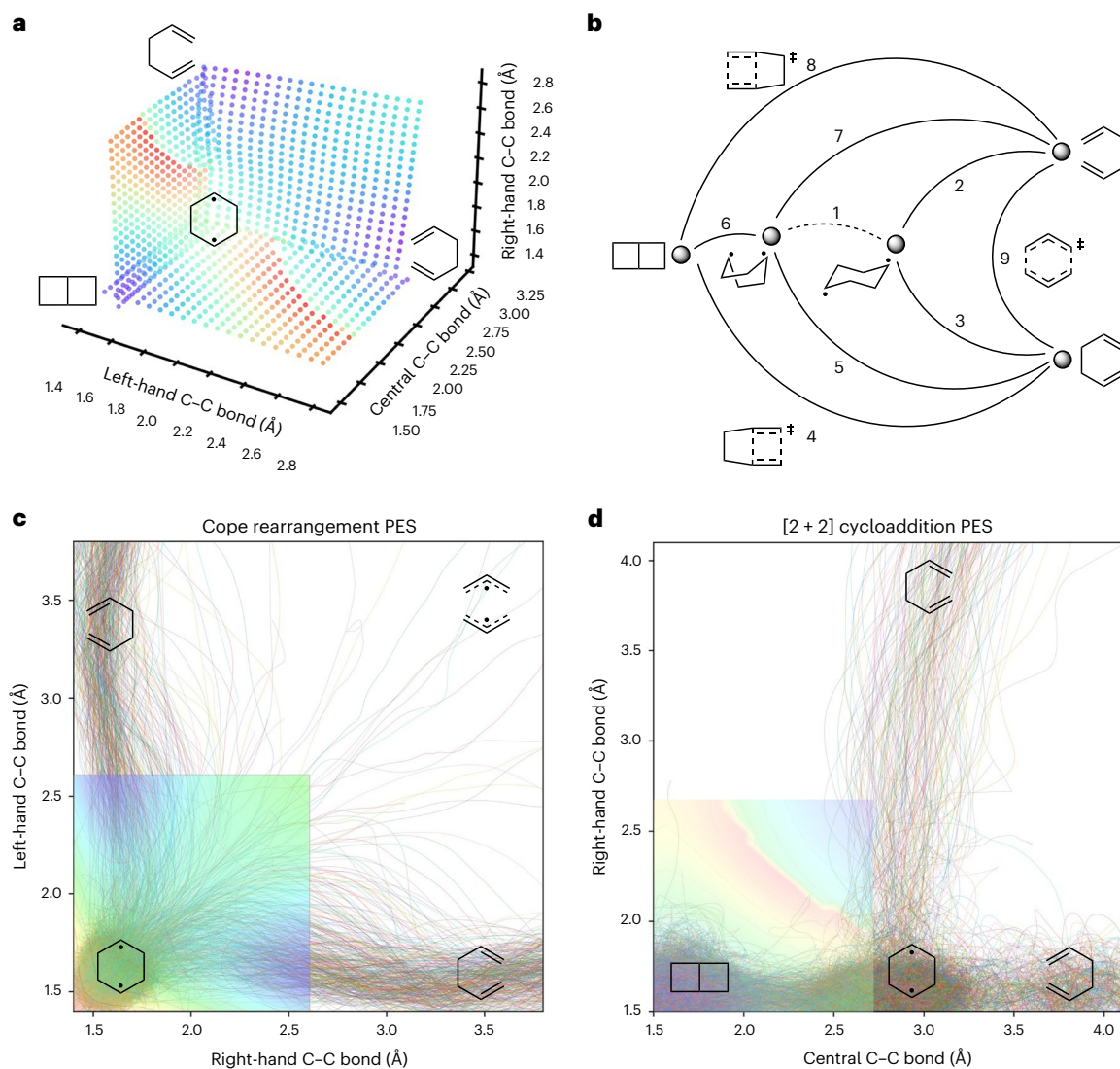


Fig. 4 | The complicated network of reactions accessible from 1,4-cyclohexanediyl. **a**, Three-dimensional PES adjacent to 1,4-cyclohexanediyl with energies indicated by colour (red indicates high energy and purple indicates low energy). Insets in all panels show chemical structures. **b**, Schematic reaction

network of cyclohexyl diradical. Pathways are labelled. **c**, Cope rearrangement branch of the PES with ML-based ab initio MD (ML-AIMD) trajectories. **d**, The [2 + 2] cycloaddition branch of the PES with ML-AIMD trajectories.

of the 1,4-cyclohexanediyl, thereby determining which products are formed as this diradical is left behind. The fate of the diradical is generally thought to depend on its conformation and spin multiplicity. For example, Anderson and Grissom proposed previously that boat conformations eventually lead to a statistical distribution of singlet and triplet diradicals, which each lead to distinct products⁴⁰. Short-lived boat conformations are thought to lead to the formation of BCH, while long-lived boat conformations undergo ISC to triplets, which then relax to energetically favoured twist-boat conformations that lead to HD products. However, both HD and BCH products were observed in our ML-NAMD simulations of pure singlets. Although we are not able to completely exclude the possibility of contributions from triplet reactions, the prior conformation–reactivity model appears to be in need of modification.

The conformations of the 1,4-cyclohexanediyl can be described by two dihedral angles (*A* and *B*), as illustrated in Fig. 3 (top left). Each dihedral angle has three different operations: CW rotation (the dihedral angle rotates clockwise), CCW rotation (the dihedral angle rotates counterclockwise) and R (the dihedral angle retains its original value in the DBO reactant, which is close to 0). There are three extreme dihedral

angles for these three operations, which we name up (U), down (D) and middle (M). In total, there are nine extreme dihedral angle pairs (Fig. 3, top right). The four structures on the two axes are half-chair conformations (UM, DM, MU, MD), with their two formal singly occupied *p* orbitals approximately perpendicular to each other. The chair structures (UD and DU) are at the top right and bottom left corners, while the boat structures (UU and DD) are at the top left and bottom right. The transition structure for the first C–N bond dissociation, which resides near the centre of this plot, is MM.

To address the relationship between the diradical conformation and the product distribution, we analysed the dihedral angle evolution along trajectories initiated from the transition structure for breaking the first C–N bond. To distinguish the two reaction pathways (towards BCH and towards HD), we plotted the population difference of the dihedral angles for a given time frame (Fig. 3b–j). The excess of the products is colour-coded (red indicates an excess of HD and blue indicates an excess of BCH). As the first C–N bond cleaves, dihedral *B* acquires more freedom to spread out along the *y* axis: depending on the degree of dissociation, dihedral *B* can do a CW rotation to approach the chair-like conformation (top right, UD), persist in a half-boat-like

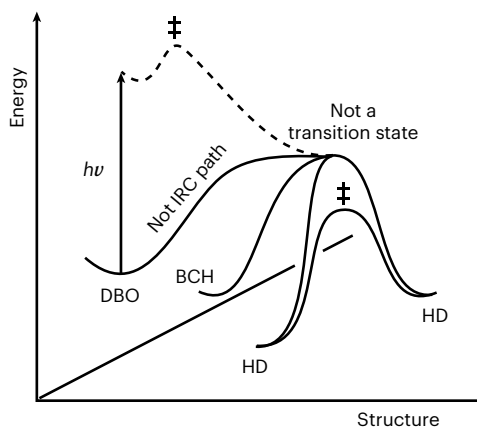


Fig. 5 | How good was our analogy? The scenario observed for DBO photolysis. Comparing this scenario to that in Fig. 1c, one can see that some aspects of the proposed scenario were captured and some were not. Nonetheless, pursuit of the design principles derived from the initial analogy led to new insights into a complex photochemical reaction. The diagonal line indicates depth, IRC, intrinsic reaction coordinate.

conformation (middle right, UM) or do a slight CCW rotation (bottom right, UU). As is evident from the separation of the blue and red regions in the first frame, the initial geometry correlates with the final product distribution. Along the propagation of the trajectories, starting from ~ 100 fs, the bifurcation of the reaction pathways leading to BCH and HD products becomes clear. Additionally, we have observed periodic ‘flips’ of blue and red regions in the first 1,800 a.u. (43 fs), which indicates a ‘recoil’ momentum arising from breaking the first C–N bond (more detailed illustrations with shorter time steps are displayed in Supplementary Fig. 14). In the first 40 fs, the recoil momentum causes dihedral angle *B* to vibrate back and forth while dihedral angle *A* is restrained by the second C–N bond.

The second C–N bond dissociates on a much shorter timescale, as the diazanyl diradical sits on the top of an exothermic downhill pathway (Fig. 2). The resulting recoil momentum from the ejection of the N_2 molecule leads to a CCW rotation of dihedral angle *A*. In the population difference plots, this manifests as an exploration of values along the $-x$ direction. Due to the exothermicity and the absence of minima along the pathway, there is effectively no time for intramolecular vibrational energy redistribution. Consequently, for the majority of the trajectories, dihedral *A* undergoes a CCW rotation, producing *exo*-BCH and *Z,E*-HD (note that we overestimate the *exo/endo* selectivity; Fig. 2d). If dihedral *B* also initially undergoes a CCW rotation, a chair-like conformation is formed. The chair-like conformation of the 1,4-cyclohexanediyl closely resembles the lower energy conformation of the transition structure for the [3, 3] sigmatropic shift^{27,28}, allowing for the formation of HD products by just a small elongation of one of the C–C bonds. By contrast, if dihedral *B* initially undergoes a CW rotation, and dihedral *A* undergoes a CCW rotation, a double-inverted boat-like conformation that quickly falls to *endo*-BCH is expected.

In short, during the breaking of the second C–N bond, the carbon that will bear the unpaired spin ‘flips away’ from the nitrogen—this motion leads to the preferred stereoisomers of the products. During that time, the distal carbon radical centre can flip twice. If, at the transition state, the distal carbon was moving in the same direction as the N-bearing carbon, then the two radical carbons end up flipped away from each other as the 1,4-cyclohexanediyl forms a chair-like structure, which tends to form HD products. Conversely, if the distal carbon was moving in the opposite direction as the N-bearing carbon, then the two radical carbons end up near to each other as the 1,4-cyclohexanediyl forms a boat-like structure, allowing those radical centres to engage in bond formation, leading to BCH products.

Multiple exit pathways from the 1,4-cyclohexanediyl

The network of pathways from the 1,4-cyclohexanediyl to BCH and HD products is complex. Two views of this network are shown in Fig. 4a,b. Figure 4a shows a three-dimensional scatter plot derived from scanning the three critical forming/breaking C–C bonds that relate the BCH and HD products. The discontinuities in energy arise from dimensionality reduction, in particular, from changing dihedral angles. The three products—BCH and two equivalent HDs—are located in the three regions of low energy, coloured blue. Separating each pair of products, there is a ridge-like region of relatively high energy, coloured red. All of the diradical conformations discussed earlier reside at the centre of the plot, as the bond length differences among these conformations are very small. Due to the small energies required for conformational changes, this region is fairly flat. Another view of this network is shown in Fig. 4b, where connectivity between key structures is emphasized. For example, the ridge-like regions in the three-dimensional scatter plot correspond to pathways 4 and 8 (for [2 + 2] cycloaddition; Fig. 4d) and pathway 9 (for a [3, 3] sigmatropic shift; Fig. 4c) in the connectivity plot. As shown in the trajectories in Fig. 4c,d, the diradicals move along one of the three ridges and fall to one of the products, depending on their initial geometries and momenta. Specifically for the [3, 3] sigmatropic shift branch, the trajectories explore different sides of the ridge before committing to one of the products, similar to behaviour observed for some reactions with ground-state PTSBs^{2–5,7}. Also of note is that some of the trajectories in Fig. 4d explore the diagonal region, which corresponds to the dissociation of the 1,4-cyclohexanediyl into two allylic radicals²⁷. In our original design, there was a single ridge and two downhill paths to the two HD products (Fig. 1d), but we find here paths to the BCH product as well.

Previously we showed, for carbocation rearrangements, that ambimodal transition states can correlate with each other, being connected by relatively flat, low-energy pathways that allow the leakage of trajectories from one to the other⁹. The scenario just described and summarized in Fig. 4 constitutes a three-dimensional example in terms of PES topography, although access to the flat interconnecting zone comes from an excited-state surface in this case (Fig. 5).

Conclusions

Using state-of-the-art ML-NAMD simulations, we have answered several lingering questions about a classical photochemical reaction: the deazetization of DBO. Perhaps most importantly, we propose a new detailed model that rationalizes the product distribution based on non-statistical dynamic effects (that is, momentum/dynamic matching effects) on the conformational behaviour of 1,4-cyclohexanediyls formed via hopping from the S_1 surface. In short, if the momentum as the 1,4-cyclohexanediyl is reached is such that rotation of dihedral *B* leads to the UM or UD conformations (Fig. 3), HD products dominate. Otherwise, BCH products form. The *exo/endo* ratio appears to be determined by the momentum associated with dihedral *A*. We do not need to invoke triplets to rationalize the experimental product distribution.

This project was initiated as a means of testing the design principle outlined in Fig. 1d: access to a transition state connecting two possible products from an excited-state surface could allow control of product ratios by non-statistical dynamic effects, in analogy to ground-state reactions involving PTSBs (Fig. 1b). We demonstrate here that photochemical deazetization of DBO does involve hopping from an excited-state surface to a ground-state surface near to a product-interconverting transition state, and the manner in which trajectories navigate from the excited state to the products is influenced by non-statistical dynamic effects—results that bode well for future design. The reaction studied here is even more complex, however, with exit routes to ladderane (BCH) products (Fig. 5); one could view the presence of an additional competing product as a problem for design or an opportunity to tune for that product. We are excited about the latter possibility.

Online content

Any methods, additional references, Nature Portfolio reporting summaries, source data, extended data, supplementary information, acknowledgements, peer review information; details of author contributions and competing interests; and statements of data and code availability are available at <https://doi.org/10.1038/s41557-023-01410-y>.

References

1. Rehbein, J. & Carpenter, B. K. Do we fully understand what controls chemical selectivity? *Phys. Chem. Chem. Phys.* **13**, 20906 (2011).
2. Ess, D. H. et al. Bifurcations on potential energy surfaces of organic reactions. *Angew. Chem. Int. Ed.* **47**, 7592–7601 (2008).
3. Martin-Somer, A., Xue, X.-S., Jamieson, C. S., Zou, Y. & Houk, K. N. Computational design of a tetrapericyclic cycloaddition and the nature of potential energy surfaces with multiple bifurcations. *J. Am. Chem. Soc.* <https://doi.org/10.1021/jacs.2c12871> (2023).
4. Campos, R. B. & Tantillo, D. J. Designing reactions with post-transition-state bifurcations: asynchronous nitrene insertions into C–C σ bonds. *Chem* **5**, 227–236 (2019).
5. Hare, S. R. & Tantillo, D. J. Post-transition state bifurcations gain momentum – current state of the field. *Pure Appl. Chem.* **89**, 679–698 (2017).
6. Guo, W., Hare, S. R., Chen, S.-S., Saunders, C. M. & Tantillo, D. J. C–H insertion in dirhodium tetracarboxylate-catalyzed reactions despite dynamical tendencies toward fragmentation: implications for reaction efficiency and catalyst design. *J. Am. Chem. Soc.* **144**, 17219–17231 (2022).
7. Hare, S. R. & Tantillo, D. J. Cryptic post-transition state bifurcations that reduce the efficiency of lactone-forming Rh-carbenoid C–H insertions. *Chem. Sci.* **8**, 1442–1449 (2017).
8. Hare, S. R. & Tantillo, D. J. Dynamic behavior of rearranging carbocations – implications for terpene biosynthesis. *Beilstein J. Org. Chem.* **12**, 377–390 (2016).
9. Feng, Z. & Tantillo, D. J. Dynamic effects on migratory aptitudes in carbocation reactions. *J. Am. Chem. Soc.* **143**, 1088–1097 (2021).
10. Bai, M., Feng, Z., Li, J. & Tantillo, D. J. Bouncing off walls – widths of exit channels from shallow minima can dominate selectivity control. *Chem. Sci.* **11**, 9937–9944 (2020).
11. Nieves-Quinones, Y. & Singleton, D. A. Dynamics and the regiochemistry of nitration of toluene. *J. Am. Chem. Soc.* **138**, 15167–15176 (2016).
12. Roytman, V. A. & Singleton, D. A. Solvation dynamics and the nature of reaction barriers and ion-pair intermediates in carbocation reactions. *J. Am. Chem. Soc.* **142**, 12865–12877 (2020).
13. Carpenter, B. K. Energy disposition in reactive intermediates. *Chem. Rev.* **113**, 7265–7286 (2013).
14. Palmer, I. J., Ragazos, I. N., Bernardi, F., Olivucci, M. & Robb, M. A. An MC-SCF study of the S1 and S2 photochemical reactions of benzene. *J. Am. Chem. Soc.* **115**, 673–682 (1993).
15. Van der Lugt, W. Th. A. M. & Oosterhoff, L. J. Symmetry control and photoinduced reactions. *J. Am. Chem. Soc.* **91**, 6042–6049 (1969).
16. Bernardi, F., Olivucci, M. & Robb, M. A. Potential energy surface crossings in organic photochemistry. *Chem. Soc. Rev.* **25**, 321–328 (1996).
17. Mai, S. & González, L. Molecular photochemistry: recent developments in theory. *Angew. Chem. Int. Ed.* **59**, 16832–16846 (2020).
18. Garavelli, M. Computational organic photochemistry: strategy, achievements and perspectives. *Theor. Chem. Acc.* **116**, 87–105 (2006).
19. Carpenter, B. K. Dynamic behavior of organic reactive intermediates. *Angew. Chem. Int. Ed.* **37**, 3340–3350 (1998).
20. Carpenter, B. K. Dynamic matching: the cause of inversion of configuration in the [1,3] sigmatropic migration? *J. Am. Chem. Soc.* **117**, 6336–6344 (1995).
21. Carpenter, B. K. Trajectories through an intermediate at a fourfold branch point. Implications for the stereochemistry of biradical reactions. *J. Am. Chem. Soc.* **107**, 5730–5732 (1985).
22. Reyes, M. B., Lobkovsky, E. B. & Carpenter, B. K. Interplay of orbital symmetry and nonstatistical dynamics in the thermal rearrangements of bicyclo[*n*.1.0]polyenes. *J. Am. Chem. Soc.* **124**, 641–651 (2002).
23. Oyola, Y. & Singleton, D. A. Dynamics and the failure of transition state theory in alkene hydroboration. *J. Am. Chem. Soc.* **131**, 3130–3131 (2009).
24. Bailey, J. O. & Singleton, D. A. Failure and redemption of statistical and nonstatistical rate theories in the hydroboration of alkenes. *J. Am. Chem. Soc.* **139**, 15710–15723 (2017).
25. Quijano, L. M. M. & Singleton, D. A. Competition between reaction and intramolecular energy redistribution in solution: observation and nature of nonstatistical dynamics in the ozonolysis of vinyl ethers. *J. Am. Chem. Soc.* **133**, 13824–13827 (2011).
26. Kuan, K.-Y. & Singleton, D. A. Vibrationally hot and cold triplets. Sensitizer-dependent dynamics and localized vibrational promotion of a di- π -methane rearrangement. *J. Am. Chem. Soc.* **142**, 19885–19888 (2020).
27. Staroverov, V. N. & Davidson, E. R. Diradical character of the Cope rearrangement transition state. *J. Am. Chem. Soc.* **122**, 186–187 (2000).
28. Doering, W. von E. & Roth, W. R. The overlap of two allyl radicals or a four-centered transition state in the Cope rearrangement. *Tetrahedron* **18**, 67–74 (1962).
29. Li, J., Stein, R. & Lopez, S. A. A theoretical stereoselectivity model of photochemical denitrogenations of diazoalkanes toward strained 1,3-dihalogenated bicyclobutanes. *J. Org. Chem.* **86**, 4061–4070 (2021).
30. Li, J. et al. Automatic discovery of photoisomerization mechanisms with nanosecond machine learning photodynamics simulations. *Chem. Sci.* **12**, 5302–5314 (2021).
31. Cox, J. M., Bain, M., Kellogg, M., Bradforth, S. E. & Lopez, S. A. Role of the perfluoro effect in the selective photochemical isomerization of hexafluorobenzene. *J. Am. Chem. Soc.* **143**, 7002–7012 (2021).
32. Li, J., Stein, R., Adrion, D. M. & Lopez, S. A. Machine-learning photodynamics simulations uncover the role of substituent effects on the photochemical formation of cubanes. *J. Am. Chem. Soc.* **143**, 20166–20175 (2021).
33. Li, J. & Lopez, S. A. Excited-state distortions promote the photochemical 4 π -electrocyclizations of fluorobenzenes via machine learning accelerated photodynamics simulations. *Chem. Eur. J.* **28**, e202200651 (2022).
34. Li, J. & Lopez, S. A. A look inside the black box of machine learning photodynamics simulations. *Acc. Chem. Res.* **55**, 1972–1984 (2022).
35. Schmidt, J. R., Parandekar, P. V. & Tully, J. C. Mixed quantum-classical equilibrium: surface hopping. *J. Chem. Phys.* **129**, 044104 (2008).
36. Lodewyk, M. W. et al. The correct structure of aquatolide—experimental validation of a theoretically-predicted structural revision. *J. Am. Chem. Soc.* **134**, 18550–18553 (2012).
37. Nouri, D. & Tantillo, D. They came from the deep: syntheses, applications, and biology of ladderanes. *Curr. Org. Chem.* **10**, 2055–2074 (2006).
38. Epplin, R. C. et al. [2]-Ladderanes as isosteres for meta-substituted aromatic rings and rigidified cyclohexanes. *Nat. Commun.* **13**, 6056 (2022).

39. Anderson, M. A. & Grissom, C. B. Increasing the heavy atom effect of xenon by adsorption to zeolites: photolysis of 2,3-diazabicyclo[2.2.2]oct-2-ene. *J. Am. Chem. Soc.* **118**, 9552–9556 (1996).
40. Anderson, M. A. & Grissom, C. B. Photolysis of 2,3-diazabicyclo[2.2.2]oct-2-ene: electronic spin determines the distribution of products. *J. Am. Chem. Soc.* **117**, 5041–5048 (1995).
41. Engel, P. S., Nalepa, C. J., Soltero, L. R., Horsey, D. W. & Keys, D. E. Photolysis of reluctant azoalkanes. Effect of structure on photochemical loss of nitrogen from 2,3-diazabicyclo[2.2.2]oct-2-ene derivatives. *J. Am. Chem. Soc.* **105**, 7108–7114 (1983).
42. Engel, P. S., Hayes, R. A., Keifer, L., Szilagyi, S. & Timberlake, J. W. Extrusion of nitrogen from cyclic and bicyclic azo compounds. *J. Am. Chem. Soc.* **100**, 1876–1882 (1978).
43. Engel, P. S. & Nalepa, C. J. Photochemical decomposition and isomerization of aliphatic azo compounds. *Pure Appl. Chem.* **52**, 2621–2632 (1980).
44. Edmunds, A. J. F. & Samuel, C. J. Photochemical deazetation of 2,3-diazabicyclo[2.2.2]oct-2-ene: pseudorotation of the cyclohexanediyl biradical. *J. Chem. Soc. Perkin Trans. 1* <https://doi.org/10.1039/p19890001267> (1989)
45. Chen, H. & Li, S. Theoretical study on the photolysis mechanism of 2,3-diazabicyclo[2.2.2]oct-2-ene. *J. Am. Chem. Soc.* **127**, 13190–13199 (2005).
46. Roberson, M. J. & Simons, J. Ab initio study of the mechanism of photolytic deazetization of 2,3-diazabicyclo[2.2.2]oct-2-ene and 2,3-diazabicyclo[2.2.1]hept-2-ene. *J. Phys. Chem. A* **101**, 2379–2383 (1997).
47. Doubleday, C., Armas, R., Walker, D., Cosgriff, C. V. & Greer, E. M. Heavy-atom tunneling calculations in thirteen organic reactions: tunneling contributions are substantial, and Bell's formula closely approximates multidimensional tunneling at ≥ 250 K. *Angew. Chem. Int. Ed.* **56**, 13099–13102 (2017).
48. Li, X., Liao, T. & Chung, L. W. Computational prediction of excited-state carbon tunneling in the two steps of triplet Zimmerman di- π -methane rearrangement. *J. Am. Chem. Soc.* **139**, 16438–16441 (2017).
49. Sponsler, M. B., Jain, R., Coms, F. D. & Dougherty, D. A. Matrix-isolation decay kinetics of triplet cyclobutanediyls. Observation of both Arrhenius behavior and heavy-atom tunneling in carbon-carbon bond-forming reactions. *J. Am. Chem. Soc.* **111**, 2240–2252 (1989).
50. Buchwalter, S. L. & Closs, G. L. Electron spin resonance and CIDNP studies on 1,3-cyclopentadiyls. A localized 1,3 carbon biradical system with a triplet ground state. Tunneling in carbon-carbon bond formation. *J. Am. Chem. Soc.* **101**, 4688–4694 (1979).
51. Mignolet, B., Curchod, B. F. E. & Martínez, T. J. Rich athermal ground-state chemistry triggered by dynamics through a conical intersection. *Angew. Chem. Int. Ed.* **128**, 15217–15220 (2016).
52. Hoyer, C. E., Ghosh, S., Truhlar, D. G. & Gagliardi, L. Multiconfiguration pair-density functional theory is as accurate as CASPT2 for electronic excitation. *J. Phys. Chem. Lett.* **7**, 586–591 (2016).
53. Gagliardi, L. et al. Multiconfiguration pair-density functional theory: a new way to treat strongly correlated systems. *Acc. Chem. Res.* **50**, 66–73 (2017).
54. Li Manni, G. et al. Multiconfiguration pair-density functional theory. *J. Chem. Theory Comput.* **10**, 3669–3680 (2014).
55. Sharma, P., Bao, J. J., Truhlar, D. G. & Gagliardi, L. Multiconfiguration pair-density functional theory. *Annu. Rev. Phys. Chem.* **72**, 541–564 (2021).
56. Widmark, P.-O., Persson, B. J. & Roos, B. O. Density matrix averaged atomic natural orbital (ANO) basis sets for correlated molecular wave functions. *Theor. Chim. Acta* **79**, 419–432 (1991).
57. Pou-Amérigo, R., Merchán, M., Nebot-Gil, I., Widmark, P.-O. & Roos, B. O. Density matrix averaged atomic natural orbital (ANO) basis sets for correlated molecular wave functions. *Theor. Chim. Acta* **92**, 149–181 (1995).
58. Widmark, P.-O., Malmqvist, P.-A. & Roos, B. O. Density matrix averaged atomic natural orbital (ANO) basis sets for correlated molecular wave functions. *Theor. Chim. Acta* **77**, 291–306 (1990).
59. Pierloot, K., Dumez, B., Widmark, P.-O. & Roos, B. O. Density matrix averaged atomic natural orbital (ANO) basis sets for correlated molecular wave functions. *Theor. Chim. Acta* **90**, 87–114 (1995).
60. Finley, J., Malmqvist, P.-Å., Roos, B. O. & Serrano-Andrés, L. The multi-state CASPT2 method. *Chem. Phys. Lett.* **288**, 299–306 (1998).
61. Penfold, T. J., Gindensperger, E., Daniel, C. & Marian, C. M. Spin-vibronic mechanism for intersystem crossing. *Chem. Rev.* **118**, 6975–7025 (2018).
62. Marian, C. M. Spin-orbit coupling and intersystem crossing in molecules. *Wiley Interdiscip. Rev. Comput. Mol. Sci.* **2**, 187–203 (2012).
63. Mai, S., Marquetand, P. & González, L. A general method to describe intersystem crossing dynamics in trajectory surface hopping. *Int. J. Quantum Chem.* **115**, 1215–1231 (2015).
64. Richter, M., Marquetand, P., González-Vázquez, J., Sola, I. & González, L. SHARC: *ab initio* molecular dynamics with surface hopping in the adiabatic representation including arbitrary couplings. *J. Chem. Theory Comput.* **7**, 1253–1258 (2011).
65. Mitchell, E. C., Scott, T. R., Bao, J. J. & Truhlar, D. G. Application of multiconfiguration pair-density functional theory to the Diels–Alder reaction. *J. Phys. Chem. A* **126**, 8834–8843 (2022).
66. Calio, P. B., Truhlar, D. G. & Gagliardi, L. Nonadiabatic molecular dynamics by multiconfiguration pair-density functional theory. *J. Chem. Theory Comput.* **18**, 614–622 (2022).
67. Chen, Z., Nieves-Quinones, Y., Waas, J. R. & Singleton, D. A. Isotope effects, dynamic matching, and solvent dynamics in a Wittig reaction. Betaines as bypassed intermediates. *J. Am. Chem. Soc.* **136**, 13122–13125 (2014).
68. Wang, L., Akimov, A. & Prezhdo, O. V. Recent progress in surface hopping: 2011–2015. *J. Phys. Chem. Lett.* **7**, 2100–2112 (2016).
69. Barbatti, M. Nonadiabatic dynamics with trajectory surface hopping method. *Wiley Interdiscip. Rev. Comput. Mol. Sci.* **1**, 620–633 (2011).
70. Tully, J. C. Molecular dynamics with electronic transitions. *J. Chem. Phys.* **93**, 1061–1071 (1990).
71. Tully, J. C. Mixed quantum–classical dynamics. *Faraday Discuss.* **110**, 407–419 (1998).
72. Zhang, T. et al. Investigations of an unexpected [2+2] photocycloaddition in the synthesis of (–)-scabrolide A from quantum mechanics calculations. *J. Org. Chem.* **87**, 14115–14124 (2022).

Publisher's note Springer Nature remains neutral with regard to jurisdictional claims in published maps and institutional affiliations.

Springer Nature or its licensor (e.g. a society or other partner) holds exclusive rights to this article under a publishing agreement with the author(s) or other rightsholder(s); author self-archiving of the accepted manuscript version of this article is solely governed by the terms of such publishing agreement and applicable law.

© The Author(s), under exclusive licence to Springer Nature Limited 2024

Methods

MC-PDFT, CASPT2 and multistate (MS)-CASSCF calculations were carried out using OpenMolcas v.21 (refs. 73,74). NEVPT2 and state-specific (SS)-CASSCF calculations were carried out with ORCA v.5.0.3 (refs. 75–80). Unless otherwise stated, all calculations were performed with MC-PDFT (revPBE)^{54,55} and the ANO-S-VDZP basis set^{56–59}. An active space of eight orbitals and eight electrons was chosen for C₆H₁₀N₂ species, and four electrons and four orbitals for 1,4-cyclohexanediyls. Multiwfn software was used for the visualization of the active orbitals⁸¹. For the ML-accelerated NAMD, we followed the general procedure developed by Lopez and coworkers for dataset generation. Model training NAMD was performed with PyRAI²MD (refs. 30,32,34). The model was trained with a dataset containing 9,670 structures, and it displays small error values for energies (mean absolute error (MAE) = 0.049 eV, coefficient of determination (R^2) = 0.9987) and gradients (MAE = 0.15 eV Å⁻¹, R^2 = 0.9923). For each simulation, 3,600 trajectories were initiated from a Wigner sampling of the transition state and the trajectories were propagated with a step size of 20 a.u. (0.48 fs). The total energy is conserved in the S₁ state, and the Nosé–Hoover thermostat is applied in the S₀ state (temperature T = 300 K). The surface hopping probability was computed based on Zhu–Nakamura theory⁸² (Supplementary Information for details of the model training, grid searching, performance and NAMD simulation).

Data availability

Additional computational data are provided as online Supplementary Information, including information on neural network model validation, comparison of theoretical methods, data on potential energy surfaces, data on surface hopping points and coordinates for computed structures.

References

73. Aquilante, F. et al. Modern quantum chemistry with [Open] Molcas. *J. Chem. Phys.* **152**, 214117 (2020).
74. Fdez. Galván, I. et al. OpenMolcas: from source code to insight. *J. Chem. Theory Comput.* **15**, 5925–5964 (2019).
75. Hellweg, A., Hättig, C., Höfener, S. & Klopper, W. Optimized accurate auxiliary basis sets for RI-MP2 and RI-CC2 calculations for the atoms Rb to Rn. *Theor. Chem. Acc.* **117**, 587–597 (2007).
76. Weigend, F. Accurate Coulomb-fitting basis sets for H to Rn. *Phys. Chem. Chem. Phys.* **8**, 1057–1065 (2006).
77. Weigend, F. & Ahlrichs, R. Balanced basis sets of split valence, triple zeta valence and quadruple zeta valence quality for H to Rn: design and assessment of accuracy. *Phys. Chem. Chem. Phys.* **7**, 3297–3305 (2005).

78. Neese, F., Wennmohs, F., Hansen, A. & Becker, U. Efficient, approximate and parallel Hartree–Fock and hybrid DFT calculations. A ‘chain-of-spheres’ algorithm for the Hartree–Fock exchange. *Chem. Phys.* **356**, 98–109 (2009).
79. Neese, F. Software update: the ORCA program system, version 4.0. *WIREs Comput. Mol. Sci.* **8**, e1327 (2018).
80. Neese, F. The ORCA program system. *WIREs Computational Molecular Science* **2**, 73–78 (2012).
81. Lu, T. & Chen, F. Multiwfn: a multifunctional wavefunction analyzer. *J. Comput. Chem.* **33**, 580–592 (2012).
82. Ishida, T., Nanbu, S. & Nakamura, H. Clarification of nonadiabatic chemical dynamics by the Zhu–Nakamura theory of nonadiabatic transition: from tri-atomic systems to reactions in solutions. *Int. Rev. Phys. Chem.* **36**, 229–285 (2017).

Acknowledgements

We gratefully acknowledge support from the National Science Foundation (CHE-1856416 and supercomputing resources from the Extreme Science and Engineering Discovery Environment (XSEDE) and Advanced Cyberinfrastructure Coordination Ecosystem: Services & Support (ACCESS) programmes to D.J.T.). The preliminary work of D.J.T. and Z.F. on photochemical modelling was supported by the American Chemical Society’s Petroleum Research Fund (ACS-PRF, PRF no. 60663-ND4). We also thank S. Lopez and J. Li for their helpful suggestions.

Author contributions

D.J.T. conceptualized the project. Z.F. designed the computational experiments with input from all authors. Z.F., W.G. and W.-Y.K. performed the calculations. All authors analysed and interpreted data. Z.F. draughted the original version of the paper. Z.F. and D.J.T. edited the paper with input from all authors.

Competing interests

The authors declare no competing interests.

Additional information

Supplementary information The online version contains supplementary material available at <https://doi.org/10.1038/s41557-023-01410-y>.

Correspondence and requests for materials should be addressed to Dean J. Tantillo.

Peer review information *Nature Chemistry* thanks Lung Wa Chung, Jingbai Li and the other, anonymous, reviewer(s) for their contribution to the peer review of this work.

Reprints and permissions information is available at www.nature.com/reprints.